V.V. YAKOVLEV✉
A. IVANOV
V. SHCHESLAVSKIY

High-energy femtosecond Cr^{4+}:forsterite oscillators and their applications in biomedical and material sciences

Department of Physics, University of Wisconsin–Milwaukee, P.O. Box 413, Milwaukee, WI 53201, USA

ABSTRACT We have designed and successfully developed a long-cavity Cr^{4+}:forsterite femtosecond oscillator, which delivers < 40 fs pulses with an energy per pulse of over 15 nJ. Complete self-starting is demonstrated. Ablation and phase transformations of semiconductor materials are achieved by the tight focusing of the laser output using a microscope objective. It is also demonstrated that Cr^{4+}:forsterite has significant advantages over Ti: sapphire for multiphoton fluorescence and coherent non-linear optical microscopy.

PACS 42.60BY; 42.62.-b; 42.65.Re; 81.70.-q; 87.50.-Hj

1   Introduction

Cr^{4+}:forsterite is a prospective laser material. Since the first demonstration of pulsed [1] and cw [2] lasing in Cr^{4+}:forsterite, it has attracted significant attention from researchers. The lasing wavelength of Cr^{4+}:forsterite is centered at 1250 nm and extends from 1100 to 1400 nm [3], making it a complimentary laser material to Ti:sapphire (lasing wavelength 700–1000 nm) and Cr^{4+}: YAG (lasing wavelength 1400–1600 nm). The region around 1250 nm is important for several reasons. First of all, this wavelength is around the zero-dispersion wavelength of optical fibers, and thus it makes Cr^{4+}:forsterite potentially important for the purpose of optical communication [4]. Secondly, light scattering in biological tissues at this wavelength is significantly reduced compared to 800 nm (center wavelength of the Ti:sapphire laser) and 1064 nm (Nd:YAG), while absorption is significantly lower than at approximately 1500 nm (the center wavelength of Cr^{4+}: YAG and Er:fiber lasers). This is why lasers utilizing wavelengths around 1200–1300 nm are important for non-invasive biological imaging [5, 6]. At wavelengths longer than 1100 nm, most of the modern semiconductor materials, such as Si, GaAs and Ge, are transparent. This makes possible non-linear optical imaging through relatively thick wafers of these materials [7]. Finally, an effective parametric non-linear optical conversion in AgGaS$_2$ and AgGaSe$_2$ [8] requires the

✉ Fax: +1-414/229-5589, E-mail: yakovlev@uwm.edu

pump wavelength to be in transparent region of these materials, i.e. longer than 1200 nm. The Cr^{4+}: forsterite lasing wavelength also satisfies this requirement. In addition to the above advantages, Cr^{4+}:forsterite has a very broad absorption spectrum and can be conveniently pumped by a Nd:YAG laser (1064 nm), Ti:sapphire and diode lasers (800–1000 nm) [3].

Despite of the all the beneficial properties of the Cr^{4+}: forsterite material, there are also significant shortcomings. First of all, the figure of merit (F.O.M.) of this material, generally defined as the ratio of absorption at the pump and lasing wavelengths, is not as high as for Ti:sapphire. The best crystals known to us have a F.O.M of approximately 30, which is at least an order of magnitude lower than that for the best Ti:sapphire crystals. In addition to the crystal quality, forsterite has a thermal conductivity coefficient significantly lower than that of Ti:sapphire. This makes alignment very sensitive to the thermal lens induced by the high average-power pump beam [9–12]. In addition, the excited state absorption may be significant, especially for the pulsed operation of a Cr^{4+}:forsterite laser [13]. Despite the above difficulties, the 10-year history of the development of this material has resulted in significant progress. As much as 3 W of cw power has been reported for the cryogenic operation of a Cr^{4+}:forsterite laser [14], while at room temperature, 1.1 W of cw power can be achieved [11]. The mode-locking regime of operation has been demonstrated [15], and by careful dispersion compensation [16, 17] pulses as short as approximately 20–25 fs can be generated, with the record now standing at a 14 fs pulse duration [18]. A typical oscillator produces pulses at a 100 MHz repetition rate, with energies of the order of 1–2 nJ. There are many applications for short-pulse lasers, such as non-linear optical imaging [19] and micromachining [20], which require higher energies. Cavity dumping of the Cr^{4+}:forsterite femtosecond laser has been demonstrated and energies as much as 30 nJ are generated at variable repetition rates [21]. An alternative way to increase the energy up to 200 μJ is to amplify the pulses [22, 23]. While very energetic pulses can be produced, this approach is expensive and leads to significant overall complexity. In this work, we adopted an extended-cavity design to decrease the repetition rate and to increase the energy per pulse. However, the low gain and poor thermal properties of Cr^{4+}:forsterite introduced signifi-

cant complications compared to the high-gain Ti:sapphire medium.

Recently, Cho et al. [24] have demonstrated a multi-pass cavity inserted inside a femtosecond Ti:sapphire oscillator, which increases the round trip time in the cavity. However, this approach is not applicable to Cr^{4+}:forsterite since accumulated losses at the mirrors will result in a significant reduction of the output power. Instead, we used the rather simple approach suggested in [25]. A simple $1:1$ telescope composed of two concave mirrors is introduced, minimizing the number of passive optical components. In this way, we constructed a high-energy femtosecond Cr^{4+}:forsterite oscillator [26], the design of which is described in detail in Sect. 2. Section 3 is devoted to possible applications of this laser in materials science and biology.

2   Laser design

2.1   *Optimization of continuous-wave operation*

The first step in designing a Cr^{4+}:forsterite laser is choosing the proper pump source. Cr^{4+}:forsterite can be pumped at several wavelengths, but the most successful operation has been demonstrated for a pump wavelength around $1 \mu m$. Typically, a Nd:YAG laser is used for this purpose. Recent progress in diode-pumped lasers makes Nd:YAG lasers a very good choice for stable, reliable pumping. However, we find several complications in using these lasers – relatively bulky sizes, relatively short lifetime of the pump diodes (typically $< 10\,000\,h$), and, sometimes, mode beating. This is why we are trying to evaluate alternative laser sources to pump the Cr^{4+}:forsterite laser. We find that the Yb:fiber laser is a very good substitution for the Nd:YAG laser. First of all, it is extremely compact – the actual size of the laser is comparable to a shoebox. Secondly, the laser intrinsically does not have a mode-beating problem and has a noise level less than 0.1%. The third reason for using a Yb:fiber laser is the much longer lifetime of the diodes ($100\,000\,h$, compared to approximately $10\,000\,h$ for the 808 nm diodes used to pump the Nd:YAG laser). Finally, the cost of the laser is approximately 50% less than the same average power (10 W, polarized output) diode-pumped Nd:YAG laser. We used the Yb:fiber laser by IPG Photonics, which delivered up to 10 W of polarized output in a single transversal mode. The output was typically collimated to a beam of approximately 4 mm in diameter.

The choice of Cr^{4+}:forsterite laser crystal is absolutely critical for the proper performance and high-power operation of this laser. For our initial studies, we used a highly doped Cr^{4+}: forsterite crystal (absorption at 1064 nm was measured to be approximately $1.6\,cm^{-1}$), grown by the Czochralski technique. The crystal we used for our experiments was Brewster cut and had dimensions of $6\,mm \times 3\,mm \times 3\,mm$ along the crystallographic a, b and c axes, respectively (in P*bmn* notation). We measured the figure of merit, i.e. the ratio of absorptions at 1064 nm and 1250 nm, to be around 12 for beams propagating along the a and polarized along the b axes. The Cr^{4+}:forsterite crystal was placed in a cooling mount and its outside temperature was stabilized to within $0.5\,°C$ at any given temperature. To test the performance of

this crystal, we constructed a simple conventional astigmatically compensated Z-fold four-mirror cavity with an optical length of approximately 140 cm, schematically shown in Fig. 1. M2 and M3 are curved mirrors ($R > 99.9\%$ from 1150 to 1400 nm, and $T > 90\%$ at 1064 nm) with a radius of curvature of 10 cm, M1 is a flat high reflector ($R > 99.9\%$ from 1150 to 1400 nm) and M4 is a 4.5% output coupler. The cw radiation of the pump beam at 1064 nm was focused through a folding mirror by the lens L, with a focal length of 10 cm. For our experimental set-up configuration, we measured the spot diameter of the pump beam to be approximately $30 \mu m$ (FWHM) at the focal point of lens L. For any given pump power and crystal temperature we optimized the focusing of the pump laser radiation (position of the lens L), the relative position of the crystal between the curved mirrors and the relative position of mirrors M2 and M3. This way, we ensured that any effects due to thermal lensing were minimized. Under these conditions, we measured the output power of the laser as a function of pump power and crystal temperature. The efficiency curves for different crystal temperatures are shown in Fig. 2. It is clearly seen that the laser output is saturated at higher pump powers and that both the output and saturation powers strongly depend on the crystal temperature. Since we excluded the effect of the thermal lens, we tried to evaluate other possible mechanisms for this saturation. We measured the luminescence dependence, in the region 1100–1500 nm, on both the temperature and the pump power under the same experimental conditions as described above for our laser configuration. As a first step, we measured the optical transmission of our Cr^{4+}:forsterite crystal for different pump powers. We found that for all the temperatures and all the pump intensities, the absorption of the Cr^{4+}:forsterite crystal at the pump wavelength remained
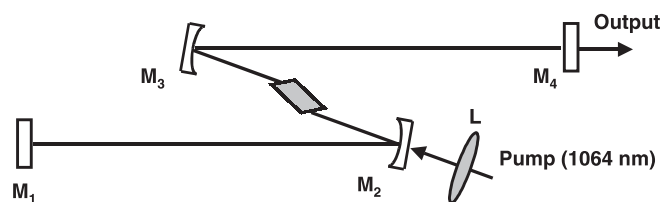

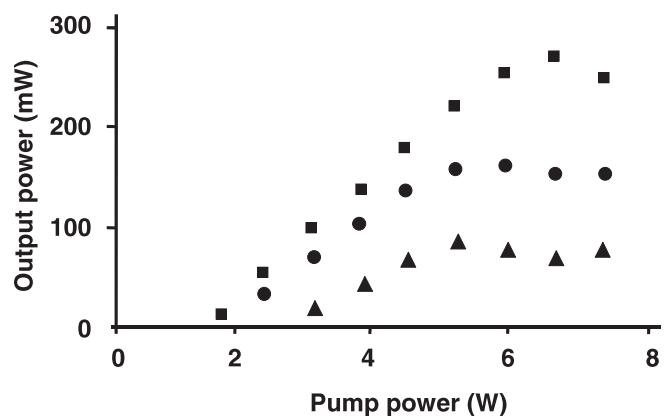**FIGURE 1**   Experimental layout of the cw Cr^{4+}: forsterite laser

FIGURE 2   Output power of the cw Cr^{4+}: forsterite laser a function of pump power (1064 nm) for different crystal holder temperatures: $t = 1.5\,°C$ (*squares*); $t = 6.5\,°C$ (*circles*); and $t = 16.5\,°C$ (*triangles*)

the same – (65±3%). These data confirm that we did not have any pump saturation absorption under our experimental conditions.

In order to confirm our hypothesis that the degradation of laser power is solely due to fluorescence quenching, we removed the crystal from the laser cavity and measured the fluorescence yield as a function of both pump power and crystal temperature [27, 28]. A similar problem has also been recently discussed with respect to another material of poor thermal quality – Cr^{3+}: LiSaF [29]. We found that for all operating crystal temperatures down to 0°C, the spectrally integrated fluorescence per unit pump power went down with increasing pump power. This effect can be easily understood if we account for the temperature in the local volume, i.e. in the excitation volume, which absorbs the input laser radiation and is responsible for fluorescence emission. We call this temperature the "local temperature", and we find that a simple formula describes the temperature difference, ΔT, between "local temperature" and the temperature of the crystal surface, t,

$$\Delta T = K P_{pump}[W] \; , \tag{1}$$

where P_{pump} is the absorbed pump power in watts, and K is a coefficient, described in [30], which can be calculated for our experimental conditions to be 12 °C/W. When this temperature is taken into account, the fluorescence yield can be described using a conventional "activation" model [31] and is given by a general formula:

$$P_{luminescence} \propto \frac{P_{pump}}{1 + C \exp(-E_a \Theta)} \tag{2}$$

where C is a fitting parameter, Θ is the inverse temperature ($\Theta = 1/(273, 15 + t + \Delta T)$) and E_a is the activation energy for non-radiative relaxation, which we estimate from the slopes of the curves to be approximately 200 meV. There is quite a good agreement between (1) and (2) and all the sets of experimental data [27, 28], which made us believe in the accuracy of our assumptions.

A significant result of these findings is that in the case of Cr^{4+}:forsterite, simple cooling, even to 0 °C, is not sufficient to avoid saturation effects and degradation of laser performance. In order to reduce this effect, a longer crystal with lower doping has to be used. In this way, the absorbed heat is distributed over the longer distance and the temperature in the focal volume is reduced. We used a 20 mm-long Cr^{4+}:forsterite crystal with approximately 60% absorption at 1064 nm. Higher doping would have lead to localization of the excitation volume and temperature increase. Our crystal had a measured figure of merit of approximately 18. We noted that the best reported results were obtained with better quality crystals [11]. The crystal was placed into a thermoelectrically cooled copper mount, and the temperature of this mount was actively stabilized. The flow of dry nitrogen helped to avoid condensation of water vapor on the surface of the crystal. This allowed the crystal mount to be cooled to temperatures as low as −6 °C without any condensation forming on the crystal surface. For most of the experiments, we varied the temperature of the crystal holder from 0 to 15 °C. To check the effect of power saturation,

we once again built a simple symmetrical four-mirror cavity. Two curved mirrors around the Cr^{4+}:forsterite crystal had a radius of curvature of 100 mm, and were high-reflectors from 1100 to 1400 nm, with approximately 87% transmission at 1064 nm. We measured the total losses of our pump laser power from its input to the surface of Cr^{4+}:forsterite crystal to be about 15%. We used a 10-cm focal length lens, AR-coated for 1064 nm, to focus the pump radiation into the laser crystal. This focusing geometry corresponded to the experimentally found optimal overlap of the pump and laser beams inside the Cr^{4+}:forsterite crystal. The length of each arm in our resonator was approximately 75 cm. The transmission of the output coupler was varied from 2.2 to 8%. The output characteristics of this laser, for optimal alignment, are shown in Fig. 3. The maximum slope efficiency for absorbed pump power is found to be over 20% for the 8% output
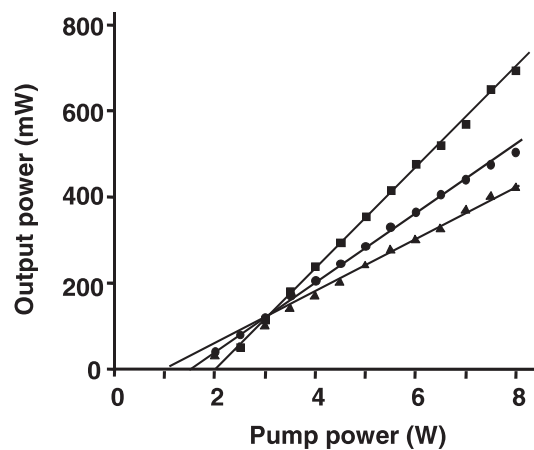
FIGURE 3   Output power of a cw Cr^{4+}: forsterite laser pumped with a Yb:fiber (1064 nm) laser for different output couplers: *squares* – 8% (slope efficiency 22%), *circles* – 3.5% (slope efficiency 15%), *triangles* – 2.2% (slope efficiency 11%). The pump power was measured after the focusing optics. The crystal holder temperature was fixed at 0 °C. Slope efficiency is defined as the ratio of output power to absorbed power
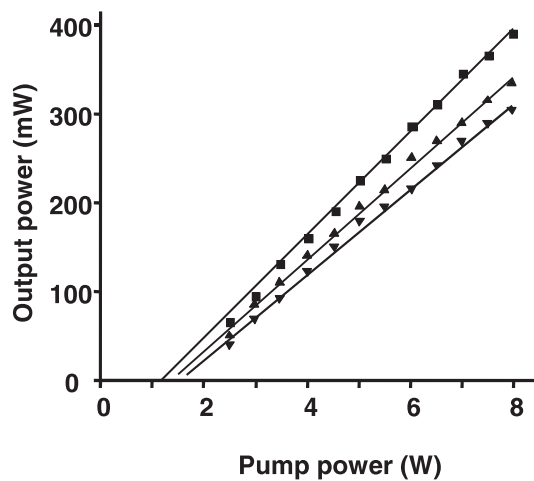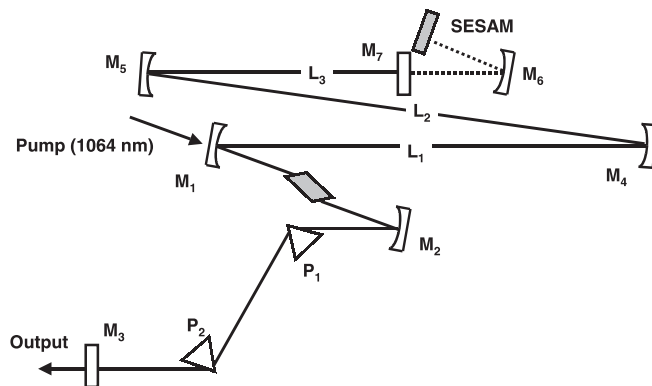

FIGURE 4   The output power of a cw Cr^{4+}: forsterite laser for different crystal holder temperatures: *squares* 0 °C (slope efficiency 11%), *triangles* 10 °C (slope efficiency 9.5%), *inverted triangles* 15 °C (slope efficiency 8.6%). The pump power was measured after the focusing optics. An output coupler with 2.2% transmission at 1250 nm was used. *Solid lines* are drawn as a guide to the eye. Slope efficiency is defined as the ratio of output power to absorbed power

coupler. For higher crystal holder temperatures, we observed a degradation of the output power – approximately 10% reduction of power for each 5 °C increase (see, for example, Fig. 4). At the lowest temperature, we did not see any saturation of the output power for the maximum input pump power used. Even at the highest pump powers, the saturation of pump absorption was negligible and was hardly measurable.

2.2   *Mode-locking regime of the* Cr^{4+}:*forsterite laser*

To achieve mode locking, we introduced a pair of SF-6 prisms for dispersion compensation. For an optimal prism position, we were able to achieve mode locking with as much as 550 mW of average power for a laser resonator approximately 160 cm-long and with a 6% output coupler. This corresponded to a pulse energy of approximately 5.9 nJ. The measured pulse duration was approximately 35 fs. We were also able to achieve mode locking with other output couplers. In the case of the 8% output coupler, the mode locking was hard to achieve and to maintain for a long time, while for the 3.5% output coupler, the output average power was significantly reduced to approximately 350 mW. To increase the pulse energy, we built a long-cavity Cr^{4+}:forsterite laser, shown in Fig. 5. The curvature of the concave mirrors (M_1 and M_2), incorporated to lengthen the cavity, was 200 cm. The length of the cavity was about 11.3 m, which corresponded to 26.5 MHz. Dispersion was compensated for by a pair of SF-6 prisms, separated by a distance of 38 cm. The output was taken from the dispersive end of the laser. An identical pair of SF-6 prisms was used to avoid the spatial distribution of the different components of the beam and to compensate for the dispersion of the output mirror and beam splitter in the autocorrelator (5-mm-thick and 1-mm-thick BK-7 substrates, respectively), before sending the pulse to an autocorrelator (we used a 0.5-mm-thick BBO crystal for all the pulse measurements).

With a 3.5% output coupler, we achieved as much as 450 mW of mode-locking power at 6.1 W of absorbed pump power and at a crystal holder temperature of –6 °C. The
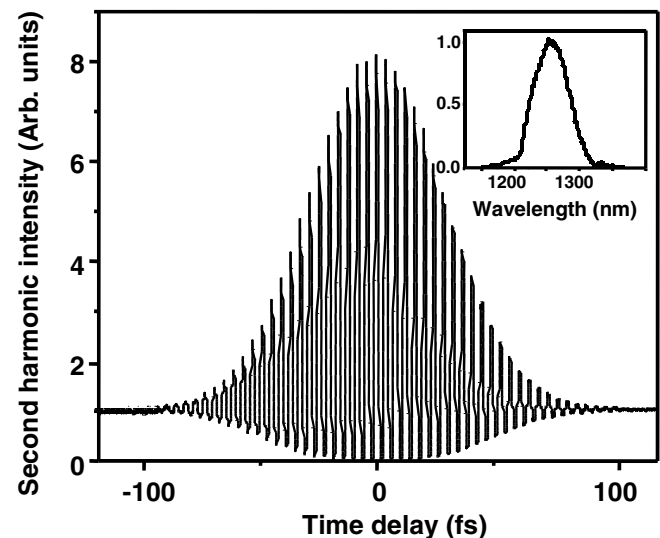
mode-locking regime appeared to be very stable and was easy to achieve by a slight knocking of the optical table or by pushing one of the prisms inside the oscillator. In fact, this long-cavity Cr^{4+}:forsterite laser was as easy to maintain and mode-lock as a conventional Ti:sapphire oscillator. The output spectrum and autocorrelation of these pulses are shown in Fig. 6. The pulses correspond to 40-fs pulses, approximately, assuming a Gaussian pulse shape, and have a time–bandwidth product of about 0.46, i.e. we have the potential of producing even shorter pulses if appropriate dispersion-compensating optics are used. The spectrum of these pulses showed excellent stability and reproducibility.

We also explored the sensitivity of mode locking on the proper alignment of the reflective-mirror telescope inside the laser cavity. Table 1 represents our results with different resonator configurations. L_1 denotes the distance from the 10-cm curved mirror to the first 200-cm curved mirror, L_2 the distance between the 200-cm curved mirrors, and L_3 the distance between the second 200-cm curved mirror and the end mirror. From this table we see that for all these configurations we were able to achieve a stable mode-locking regime with some sacrifice of the output power.

L_1 cm	L_2 cm	L_3 cm	Maximum cw output power, mW	Output power in femtosecond regime, mW	Repetition rate, (MHz)	Energy, per pulse nJ
258	225	76	250	140	23.2	6.0
120	137	22	400	130	41.0	3.2
304	200	0	430	180	25.4	7.1

TABLE 1   Output characteristics of an extended-cavity oscillator. The temperature of the crystal holder was set at 4 °C. The output coupler with 6% transmission was used. See text and Fig. 5 for definition of $L_{1,2,3}$

To achieve completely hands-off operation of our Cr^{4+}: forsterite oscillator, we introduced a SESAM mirror, based on a single InGaAs quantum well with the absorption edge

FIGURE 5   Schematic outline of the long-cavity Cr^{4+}: forsterite laser. M_1, M_2, – are 10-cm concave mirrors; M_4, M_5, 200-cm concave mirrors; and M_6, 9.3-cm concave mirror. All the other mirrors are flat. All mirrors, except the output coupler (M_3) and SESAM (SM) are high reflectors for 1100–1400 nm. L, focusing lens; and $P_{1,2}$, SF-6 prisms

FIGURE 6   An interferometric autocorrelation function and a corresponding spectrum (*inset*) of the pulses emerging from the extended cavity Cr^{4+}: forsterite oscillator for the optimal position of the extracavity prisms
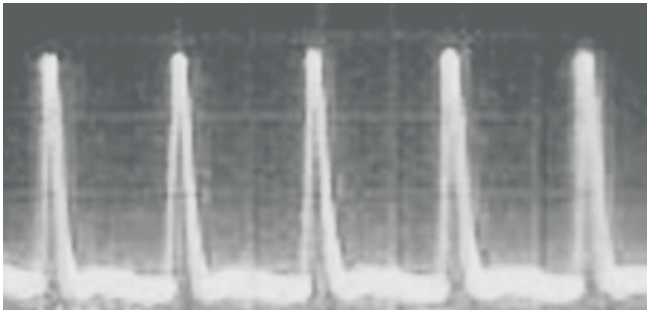
FIGURE 7   Oscilloscope trace of the pulse train from the long-cavity oscillator. Horizontal scale – 20 ns/division

at around 1230 nm. Our particular sample was not of the best quality. It introduced as much as 12% insertion loss and narrowed the spectrum. Nevertheless, we achieved very stable, self-sustained mode locking by placing the SESAM inside the cavity and focusing radiation on it with the concave mirror M_3 ($R = 9.3$ cm). The optimum separation between the focusing mirror M_3 and the SESAM was found to be 80 mm, with a tolerance ±1.5 mm. The femtosecond mode locking collapsed outside of this range. The beam size on the surface of the SESAM was estimated to be approximately 100 μm, corresponding to an incident energy density of about 750 μJ/cm^2. The output power in the mode-locked regime was 250 mW with the 6% output coupler. Decreasing the temperature of the crystal to –6 °C and increasing the absorbed pump power to 6.1 W raised the output power to 350 mW, or 13 nJ per pulse. The measured spectrum was significantly narrower, and this was reflected in the longer autocorrelation function. By our best efforts, we were only able to achieve 75 fs-long pulses.

The pulse train (Fig. 7) shows both excellent short- and long-term stability. We measured the short-term fluctuations to be 0.1% r.m.s. and observed less than 2% pulse intensity drift during a typical 12-hour run. All the output parameters (spectrum and power) were easily reproducible on a day-to-day basis.

3   Applications

The femtosecond high-energy Cr^{4+}:forsterite oscillator described in Sect. 2 has numerous applications in spectroscopy, diagnostics and micromachining. Here we outline just some of the possible directions.

3.1   *Micromachining*

With a modest microscope objective (with numerical aperture N.A.= 0.4) one can achieve a focal spot size of the order of 1.5 μm. We can generate up to 15 nJ per pulse from our extended-cavity Cr^{4+}:forsterite laser, leading to approximately 5–6 nJ in the focal spot, assuming losses in the microscope objective and delivery optics. It leads to an energy density of approximately 0.2 J/cm^2 and intensities 10^{12} W/cm^2. While these energy and power densities are not sufficient to induce transformation in transparent dielectrics (the typical damage/ablation threshold is 1 J/cm^2 [32]), they are quite sufficient to change the structure of semiconductors, which have a strong two-photon ab-

sorption. For example, by focusing the 1250-nm radiation of our laser using a 20×, N.A. = 0.4 microscope objective (Edmund Scientific Inc.), we were able to ablate the surface of silicon. Silicon is considered to be an important component of modern optoelectronics. In particular, we noted that by focusing the laser radiation through the silicon wafer (the bandgap of silicon is approximately 1 eV, and even a thick layer of silicon is transparent at 1250 nm) we could cause the transformation of the back surface of the silicon, or anywhere inside the silicon wafer. By moving the wafer in the $x - y - z$-directions, we could "write" micro-structured patterns inside the wafer with a speed of 25 million "pixels" per second (the repetition rate of the laser). The low level of noise ensured excellent reproducibility. Here, once again, we used the relative uniqueness of 1250-nm radiation compared to 800-nm radiation, which is mostly absorbed by silicon.

3.2   *Microscopic surface imaging*

Non-linear optical methods, such as second- and third-harmonic generation, are well-known spectroscopic techniques for providing structural information about the surface and surface layers of materials [33]. Since these methods are non-linear optical methods, they rely on the use of a high-intensity laser source. Typically, the Ti:sapphire laser is considered as the major source of femtosecond pulses for non-linear optical microscopy studies. We have shown an advantage of our laser by demonstrating microscopic imaging using the Cr^{4+}:forsterite oscillator. We noted that the radiation of the second harmonic ($\lambda = 625$ nm) and third harmonic ($\lambda = 417$ nm) of the Cr^{4+}: forsterite laser is in the transparent region for conventional microscope objectives, while the detection efficiency is still high compared to the third harmonic of the Ti:sapphire laser ($\lambda = 266$ nm). Moreover, most photodetectors for visible radiation are completely blind to 1250-nm radiation, making weak signal discrimination easier and less expensive (since off-the-shelf components can be used). The schematic of our experimental set-up is shown in Fig. 8. Typically, we used a 10×, N.A. = 0.2 microscope objective, since the use of a higher numerical aperture objective resulted in the damage of most of the absorbing materials. For our detection system, we used a liquid-nitrogen-cooled CCD attached to 1/4-m spectrometer. The advantage of this was that the 16-bit camera
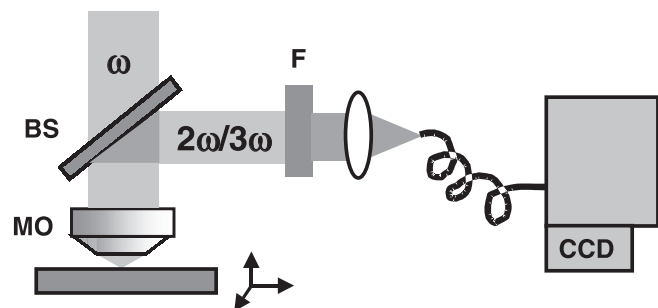
FIGURE 8   Experimental set-up for non-linear optical microscopic material characterization: BS, dichroic mirror (highly transparent at 1250 nm, highly reflective < 700 nm); MO, microscope objective; and F, filter
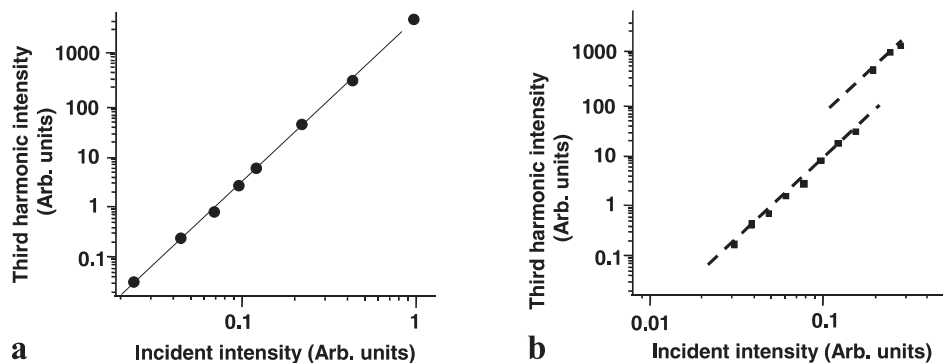
FIGURE 9 The intensity of the third harmonic generated from the surface of silicon (**a**) and VO$_2$ (**b**) as a function of the incident pulse intensity

could work in photon-counting mode if long exposure times were used. We were able to achieve over 7 orders of dynamic range of second- and third-harmonic signal detection without loosing any of the signal or linearity of detection by varying the exposure time from 0.1 to 1000 s. Figure 9a shows the intensity dependence of the third harmonic from the Si (001) wafer. Clearly, very high dynamic-range, non-linear optical measurements are possible with a simple experimental set-up. In contrast, a similar set of measurements performed with a single crystal VO$_2$ showed an interesting feature: at a certain intensity level, the third-harmonic intensity jumped abruptly, almost by orders of magnitude (Fig. 9b). Detailed analysis showed that this sudden change in the third harmonic efficiency was due to a phase transition to the conducting state [34]. Thus, for some applications, we could take advantage of the high-energy output of our oscillator. In the particular example with VO$_2$, we could study laser-induced phase transformations using a simple oscillator [34].

3.3 Biological imaging

Following its introduction in 1990 [35], multiphoton microscopy has become the most popular technique for live-cell imaging. Although the signal is much lower than in traditional single-photon fluorescence microscopy and photobleaching due to non-linear absorption may happen at a higher rate [36], one of the most significant advantages of multiphoton microscopy is its ability to probe significantly deeper layers of tissue [37]. This is due to the lower absorption and scattering at longer wavelengths used for multiphoton microscopy.

Multiphoton microscopy relies on simultaneous absorption of two or more IR quanta and thus requires high-intensity laser pulses. Traditionally, a Ti:sapphire laser is used to provide a tunable source (from 670 to 1100 nm) of femtosecond pulses ($\sim 10^{-13}$ s) at a very high repetition rate ($\sim 10^8$ Hz). Following its introduction in 1991 [38], this laser is now widely used for microscopic studies. However, we noted that there are several shortcomings of the Ti:sapphire laser, which limit its applications for biomedical imaging. Despite the often-quoted tunability range of up to 1100 nm, the most stable performance is typically achieved at around 800 nm, where there is maximum fluorescence of Ti:sapphire. A longer wavelength would benefit the multiphoton imaging from several perspectives. First of all, the scattering co-

efficient for a typical tissue [39, 40] is significantly higher than absorption coefficient in the range of wavelengths from 700 to 1300 nm, and decreases dramatically for longer wavelengths. This fact has been successfully exploited in the case of optical coherence tomography (OCT), where the use of longer wavelengths (i.e. 1250 nm compared to approximately 800 nm) results in an almost three-times increase in the probing depth of the tissue [5]. Since OCT is a linear optical technique, multiphoton imaging should benefit even more from the use of a longer wavelength. At the other end of the spectrum, water absorption peaks at approximately 1500 nm, leading to the heating of tissue in the focal volume of a laser beam [41]. Thus, the wavelength range around 1200–1300 nm is optimal for deep non-linear optical imaging of biological samples.

Dye phototoxicity is known to be a problem for long exposition times and living samples. The advantage of using a longer excitation wavelength comes with the possibility of using dyes, the two-photon absorption spectrum of which is also red-shifted. These dyes are typically less phototoxic [42]. In contrast, green fluorescent protein (GFP) [43] can be efficiently excited by a three-photon excitation process using 1250-nm radiation.

Even without the use of fluorescence markers, the high-intensity laser radiation (of the order of TW/cm^2) produced in the focus of a microscope objective presents a significant threat to living cells. As has been pointed out by several groups [44, 45], high-intensity laser radiation can affect the normal cell development process through multiphoton absorption.

One of the major motivations for using a Cr^{4+}:forsterite laser for multiphoton imaging is the assumption of a "safer" wavelength. In order to test this hypothesis, we used the embryos of Xenopus laevis [46]. We have a breeding colony of these animals, consisting of ten pairs of pigmented animals and one pair of albino, all proven breeders obtained from Nasco. Males and females were induced to mate once every 6–8 weeks by the injection of human chorionic gonadotropin (HCG) into their dorsal lymph sac [47]. An induced mating could produce from several hundred to almost two thousand fertilized eggs. Embryos were raised in aquaria. Most were raised in the colony. The few that were used for experiments were removed from the vitelline envelope and immobilized in slightly saline water on a microscope slide. Since the final goal of the multiphoton imaging of Xenopus laevis was to study the formation of functional synapses between

nerve and muscle, we found it appropriate to use the long-term development of these animals as the major indicator of the effect of high-intensity laser irradiation. For all the experiments described, we used the following procedure. Frog embryos were selected within the first 24 h. All the embryos were inspected under a regular microscope in order to ensure the proper cell divisions. Then, embryos were placed into a decompression slide in order to avoid mechanical damage and were irradiated for about 15 min by high-intensity laser pulses. The focal point of a laser beam was slowly scanned through a small portion of the embryo volume to simulate realistic imaging conditions. After irradiation, embryos were taken back to their normal environment, where they continued their development and were evaluated several days after the irradiation. We expected that as a result of the high-intensity irradiation, the embryo cell division process might be altered, and some abnormalities were expected. These abnormalities included, but not were not limited to, extra parts on the frog bodies, abnormal developments of neuronal planes and, finally, the death of embryos. These abnormalities have been well tabulated in the literature on Xenopus laevis development (see, for example, [46]), and are easily detected and registered.

We found that for the same conditions of irradiation, i.e. for the beam spot size and for the same pulse duration, longer wavelength (1250 nm) radiation produced much less damage to embryos. In fact, in a more quantitative study [47] we have demonstrated that the damage threshold (defined as the energy density at which half of the irradiated embryos have some sort of abnormalities) is an order of magnitude higher for 1250-nm radiation compared to 800-nm radiation. This fact can be explained in terms of multiphoton absorption by DNA molecules. Since DNA does not have significant absorption in the visible or near-IR, it requires a multiphoton process to absorb short-pulse irradiation. A longer wavelength higher intensity is required for multiphoton absorption. In our case, we observed quite a significant difference, which resulted in a signal difference of two orders of magnitude for any second-order non-linear process, such as two-photon fluorescence or second-harmonic generation, and three orders of signal intensity increase when the signal was determined by a third-order process, such as in non-linear Raman microscopy (CARS [48–51]) and third-harmonic-generation microscopy [52–55].

Our original motivation for using Cr^{4+}:forsterite radiation for microscopic imaging came from its potential application to conventional fluorescence microscopy. We note that other techniques that are currently attracting the attention of many research groups, such as second- and third-harmonic imaging, will benefit as well. Both the second and third harmonics of Cr^{4+}:forsterite are weakly absorbed in tissue and can be detected simultaneously in "forward" geometry, while the scattered fluorescence is collected in a reflected ("back") geometry [56].

4   Conclusion

In conclusion, we have designed and constructed a high-power Cr^{4+}:forsterite laser. It has been shown that by using a low-doped active material, a high average power output of the Cr^{4+}:forsterite oscillator can be obtained without cryogenic cooling. We have also demonstrated for the first time the extended laser cavity design for a femtosecond self-starting Cr^{4+}:forsterite laser. We were able to generate 40-fs pulses with energies as high as 17 nJ. By using moderate power microscope objectives, intensities as high as 10^{13} W/cm^2 could be achieved. It is demonstrated that this is sufficient energy for micromachining of semiconductor materials, which have a strong two-photon absorption at this wavelength. The high repetition rate and high stability of the laser source developed, combined with a friendly laser wavelength, for which the second and third harmonics lie in the visible part of the spectrum, makes the high-energy Cr^{4+}:forsterite laser an attractive instrument for non-linear optical diagnostics of materials. Finally, we have demonstrated that Cr^{4+}:forsterite radiation has several advantages compared to radiation from the conventional Ti:sapphire laser for the purpose of multiphoton fluorescence and coherent non-linear optical microscopy. In particular, the damage threshold for living tissues has been found to increase by more than an order magnitude for 1250 nm compared to 800 nm short-pulse irradiation. We believe that the high-energy Cr^{4+}:forsterite oscillators developed may find some other applications, where the choice of wavelength, energy, and repetition rate is critical.

REFERENCES

1 V. Petricevic, S.K. Gayen, R.R. Alfano, K. Yamagishi, H. Anzai, Y. Yamaguchi: Appl. Phys. Lett. **52**, 1040 (1988)
2 V. Petricevic, S.K. Gayen, R.R. Alfano: Opt. Lett. **14**, 612 (1989)
3 T.J. Carrig, C.R. Pollock: IEEE J. Quantum Electron. **QE-29**, 2835 (1993)
4 H. Shimizu, K. Kumada, N. Yamanaka, N. Iwai, T. Mukaihara, A. Kasakawa: IEEE J. Quantum Electron. **QE-36**, 728 (2000)
5 B. Golubovich, B.E. Bouma, G.J. Tearney, J.G. Fujimoto: Opt. Lett. **22**, 1704 (1997)
6 E. Abraham, E. Bordenave, N. Tsurumachi, G. Jonusauskas, J. Oberle, C. Rulliere: Opt. Lett. **25**, 929 (2000)
7 C. Xu, W. Denk: Appl. Phys. Lett. **71**, 2578 (1997)
8 F. Rotermund, V. Petrov: Opt. Lett. **25**, 746 (2000)
9 T. McKinnie, L.A.W. Gloster, Z.X. Jiang, T.A. King: Appl. Opt. **35**, 4159 (1996)
10 A. Agnesi, E. Piccinini, G.C. Reali: Opt. Commun. **135**, 77 (1997)
11 N. Zhavoronkov, A. Avtukh, V. Mikhailov: Appl. Opt. **36**, 8601 (1997)
12 A. Sennaroglu, B. Pekerten: IEEE J. Quantum Electron. **QE-34**, 1996 (1998)
13 H.R. Verdun, L. Merkle: OSA Proc. Adv. Solid-State Lasers **10**, 35 (1991)
14 T.J. Carrig, C.R. Pollock: Opt. Lett. **16**, 1662 (1991)
15 A. Seas, V. Petricevic, R.R. Alfano: Opt. Lett. **17**, 937 (1992)
16 V. Yanovsky, Y. Pang, F. Wise, B. Minkov: Opt. Lett. **18**, 1541 (1993)
17 Z. Zhang, K. Torizuka, T. Itatani, K. Kobayashi, T. Sugaya, T. Nakagawa: IEEE J. Quantum Electron. **QE-33**, 1975 (1997)
18 C. Chudoba, J.G. Fujimoto, E.P. Ippen, H.A. Haus, U. Morgner, F.X. Kaertner, V. Scheuer, G. Angelow, T. Tscudi: Opt. Lett. **26**, 292 (2001)
19 M. Muller, J. Squier, K.R. Wilson, G.J. Brakenhoff: J. Microscopy (Oxford) **191**, 266 (1998)
20 C.B. Schaffer, A. Brodeur, J.F. Garcia, E. Mazur: Opt. Lett. **26**, 93 (2001)

21 E. Slobodchikov, J. Ma, V. Kamalov, K. Tominaga, K. Yoshihara: Opt. Lett. **21**, 354 (1996)
22 G. Jonusauskas, J. Oberle, C. Rulliere: Opt. Lett. **23**, 1918 (1998)
23 V. Shcheslavskiy, N. Zhavoronkov, V. Petrov, F. Noack, M. Bouvier: IEEE J. Quantum Electron. **QE-35**, 1123 (1999)
24 S.H. Cho, B.E. Bouma, E.P. Ippen, J.G. Fujimoto: Opt. Lett **24**, 417 (1999)
25 R. Libertun, R. Shelton, H.C. Kapteyn, M.M. Murnane: CLEO Proc. CThR3, 469 (1999)
26 V. Shcheslavskiy, V.V. Yakovlev, A.A. Ivanov: Opt. Lett. **26**, 1999 (2001)
27 V.V. Yakovlev, A.A. Ivanov, V. Shcheslavskiy, A.B. Vasilyev, B.I. Minkov: Proc. SPIE **4267**, 46 (2001)
28 A.A. Ivanov, V. Shcheslavskiy, V.V. Yakovlev, A.B. Vasilyev, B.I. Minkov: Appl. Opt. **40**, 6034 (2001)
29 F. Balembois, F. Kerboull, F. Druon, F. Falcoz, P. Geroges, A. Brun: IEEE J. Quantum Electron. **QE-33**, 269 (1997)
30 A. Ivanov, B. Minkov, G. Jonusauskas, J. Oberle, C. Rulliere: Opt. Commun. **116**, 131 (1995)
31 D. Bimberg, M. Sondergeld, E. Grobe: Phys. Rev. B **48**, 3451 (1971)
32 M. Lezner, J. Kruger, S. Sartania, Z. Cheng, C. Spielmann, G. Mourou, W. Kautek, F. Krausz: Phys. Rev. Lett. **80**, 4076 (1998)
33 Y.R. Shen: IEEE J. Quantum Electron. **QE-6**, 1375 (2000)
34 G.I. Petrov, V.V. Yakovlev, J.A. Squier: Opt. Lett. **27**, 655 (2001)
35 W. Denk, J.H. Strickler, W.W. Webb: Science **248**, 73 (1990)
36 G.H. Patterson, D.W. Piston: Biophysical J. **78**, 2159 (2000)
37 V. Daria, O. Nakamura, C. Palmes-Saloma, S. Kawat: Jap. J. Appl. Phys. **37**, L959 (1998)
38 D.E. Spence, P.N. Kean, W. Sibbett: Opt. Lett. **16**, 42 (1991)
39 P. Parsa, S. Jacques, N. Nishioka: Appl. Opt. **28**, 2325 (1989)
40 V. Tuchin: *Tissue Optics* (SPIE Press, Bellingham 2000)
41 A. Schonle, S.W. Hell: Opt. Lett. **23**, 325 (1998)
42 R.P. Haugland (Ed.): *Handbook of Fluorescent Probes and Research Chemicals* (Molecular Probes, Eugene 1997)
43 R.Y. Tsien: Annu. Rev. Biochem. **67**, 509 (1998)
44 K. Konig, I. Riemann, P. Fischer, T. Becker, H. Oehring, K.J. Halbhuber: Proc. SPIE **3616**, 100 (1999)
45 K. Konig, P. So, W.W. Mantulin, E. Gratton: Opt. Lett. **22**, 135 (1997)
46 J.B. Gurdon: "African clawed frogs" *Methods in Developmental Biology*, Ed. by F.H. Wilt, N.K. Wessells (Crowell, New York 1982) pp. 75–84
47 V. Shcheslavskii, A. Ivanov, D. Heathcote, V. Yakovlev: Proc. SPIE **4262**, 192 (2001)
48 A. Zumbusch, G.R. Holton, X.S. Xie: Phys. Rev. Lett. **82**, 4142 (1999)
49 M. Muller, J. Squier, C.A. De Lange, G.J. Brakenhoff: J. Microscopy **197**, 150 (2000)
50 E.O. Potma, W.P. de Boeij, D.A. Wiersma: J. Opt. Soc. Am. B **17**, 1678 (2000)
51 V. Yakovlev: Proc. SPIE **4254**, 97 (2001)
52 Y. Guo, P.P. Ho, F. Liu, R.R. Alfano: Appl. Opt. **35**, 6810 (1996)
53 Y. Barad, H. Eisenberg, M. Horowitz, Y. Silberberg: Appl. Phys. Lett. **70**, 922 (1997)
54 M. Muller, J. Squier, K.R. Wilson, G.J. Brakenhoff: J. Microscopy **191**, 266 (1998)
55 G. Peleg, A. Lewis, M. Linial, L.M. Loew: Proc. Natl. Acad. Sci. USA **96**, 6700 (1999)
56 P.C. Cheng, C.K. Sun, B.L. Lin, F.J. Kao, S.W. Chu: Proc. SPIE **4262**, 98 (2001)